Large Eddy Simulation of medium-scale methanol pool fires - effects of pool boundary conditions

Li Ma, Fatiha Nmira, Jean-Louis Consalvi

Large Eddy Simulation of medium-scale methanol pool fires - effects of pool boundary conditions

Li Ma, Fatiha Nmira, Jean-Louis Consalvi

Large Eddy Simulation of medium-scale methanol pool fires - effects of pool boundary conditions

Li Ma[a,b], Fatiha Nmira[a], Jean-Louis Consalvi [b,*]

[a] *Direction R&D EDF, 6 Quai Watier, 78401, Chatou Cedex, France*
[b] *Aix-Marseille Université, IUSTI/UMR CNRS 7343, 5 rue E. Fermi, 13453 Marseille Cedex 13, France*

Abstract

This article reports Large Eddy Simulation (LES) of 30 cm diameter methanol pool fires in order to investigate the effects of the burner boundary conditions on the pool dynamics. The numerical model involves state-of-the-art subgrid scale (SGS) sub-models for mixing, combustion and turbulence-radiation interaction with all the model constants computed dynamically. The non-adiabatic steady laminar flamelet (SLF)/presumed filtered density function (FDF) combustion model is used whereas the radiation model combines the Rank Correlated Full Spectrum k-distribution (RCFSK) for spectral radiation with the finite volume method (FVM) as radiative transfer equation (RTE) solver. The baseline case considers a burner located one-pool diameter above the floor and a fuel lip height of 1 cm as specified in the experiments used for model validation. Model predictions for puffing frequency, mean and rms temperature and velocity, mean molar fractions of major species, radiative loss to the surrounding and radiative and total heat feedback to

*Corresponding author
Email addresses: li.ma@edf.fr (Li Ma), fatiha.nmira@edf.fr (Fatiha Nmira), jean-louis.consalvi@univ-amu.fr (Jean-Louis Consalvi)

the fuel surface are in good agreement with the available experimental data. Two other burner boundary conditions are designed. The first disregards the fuel lip height while keeping the burner located one-pool diameter above the floor. The second modifies the first configuration by assuming that the burner rim is floor flush. Model results show that the burner boundary conditions affect significantly the flow structure and the pool fire dynamics by altering the flame base instability near the edge of the pan. A non-zero fuel lip height produces significantly wider and shorter flames which affect the heat feedback toward the fuel surface whereas altering the air entrainment at the pool basis enhances substantially the puffing frequency. This shows that the experimental burner boundary conditions have to be reproduced scrupulously for relevant model validations.

Keywords: Methanol pool fire, burner boundary conditions, large eddy simulation, non-adiabatic steady laminar flamelet model, Rank-Correlated Full-Spectrum k-distribution.

---

1. Introduction

Computational Fluid Dynamics models are becoming an important part of the fire protection engineering owing to the significant progress made over the last twenty years with the development of LES-based fire simulators such as FDS by the NIST and FireFoam by FM Global [1, 2]. Model validation over target configurations is a crucial step in the development of such simulators and their subsequent application to real fire problems. As such, fire plumes generated either from gaseous burners or liquid pans are natural canonical scenarios in fire safety science since they contain most of the coupled physical processes involved in fire problems, namely, buoyancy-controlled flows, buoyancy-induced turbulence, turbulent combustion, thermal radiation, soot generation, and, in the case of pool fires, burning rate [3].

Well-documented experiments relative to laboratory-scale fire plumes were reported over the time and have served for model validations [4–19]. A significant amount of LES of these fire plumes was performed in the last decade and encouraging results were reported about the capability of the numerical models to reproduce their dynamics [20–32]. Keeping in mind the objective of subsequent applications to industrial fires, most of these studies have considered a simple one-step irreversible reaction, coupled either to the eddy dissipation concept or a presumed FDF approach, as well as simplified radiative heat transfer models involving either a constant radiant fraction or a grey model. Finer descriptions of combustion and spectral radiation were considered by Wu et al. [32] in order to simulate the 7.1 cm heptane pool fire investigated experimentally by Klassen and Gore [11]. In their simulations, turbulence was fully resolved by the grid whereas a 33-species skeletal

mechanism and a two-equation acetylene-based model were used to model chemistry and soot production, respectively. Radiation was modeled using the Line-by-Line Photon Monte Carlo method proposed by Wang and Modest [33], and the contributions of CO_2, H_2O, CO, CH_4, C_2H_4 and soot were taken into account.

On the other hand, experimental studies revealed the importance of burner boundary conditions on the fire plume dynamics. Orloff [34] and Orloff and de Ris [35] observed that the fuel lip height, defined as the fuel level below the burner rim, has significant effects on the fire plume structure. A non-zero lip height was found to result in thicker and shorter fires [34], which was attributed to effects on the transition to turbulence [35, 36]. Weckman and Sobiesiak [10] considered different burner arrangements in medium-scale acetone pool fires in order to modify the air entrainment at the pool basis. They found that the puffing frequency as well as the behaviour of large-scale structures are extremely dependent on the burner boundary conditions and recommended to specify them in future experimental works. In most of the experimental studies of pool fires and fire plumes published to date, a great attention was generally paid to the design of the burner boundary conditions and a detailed description was provided. From the early works of McCaffrey [4], Cox and Chitty [5–7] and Crauford et al. [8], the burner is generally set at least one-pool diameter above the floor to minimize the effects of surrounding surfaces on the fire behavior. In the case of pool fires, the descriptions of the experimental set-up report also the fuel lip height. Nevertheless, burner boundary conditions in most of the modelling studies of fire plumes are either not consistent with the experiments considered for

comparison [30, 32] or not specified. Exceptions are the works of Chatterjee et al. [27] and Maragkos et al. [29]. Chatterjee et al. [27] simulated the 30 cm heptane pool fire investigated experimentally by Klassen and Gore [11]. The burner was 15 cm above the floor in line with the experimental setup but the authors did not mention if the experimental fuel lip height of 5 mm was reproduced. Maragkos et al. [29] simulated the 30 cm methanol pool fire investigated experimentally by Weckman and Strong [12]. They reported that it was important to reproduce the experimental fuel lip height in order to capture the pool dynamics. However, they did not specify if they considered a burner located one-pool diameter above the floor as in the experiments.

The objective of this article is twofold. The first aim is to assess the capability of a LES-based numerical model involving state-of-the art SGS models for turbulent mixing, combustion, and radiation to reproduce the dynamics of medium-scale methanol pool fires. The second objective is to investigate the effects of burner boundary conditions on the predictions. A special attention will be paid to the influence of the fuel lip height and on floor effects. To the authors' best knowledge, such a numerical evaluation was not reported in the literature. The article is organized as follows. The second section describes the numerical model. Numerical results are compared with the available experimental data and burner boundary condition effects are analyzed in section 3. Eventually, the conclusions drawn from the present study are summarized.

2. Numerical and physical models

2.1. Governing equations

LES is based on a separation of scales. This separation is commonly introduced by a filtering operation which decomposes the velocity and scalar fields into a resolved (filtered) part and an unresolved (SGS) part. In addition, for variable density flow, the resolved quantities are density-weighted (Favre filtered) as defined by $\bar{\rho}\tilde{\phi} = \overline{\rho\phi}$. $\bar{(\cdot)}$ and $\tilde{(\cdot)}$ represent filtered and density-weighted filtered quantities, respectively. The Favre-filtered Navier-Stokes equations supplemented with transport equations for the filtered enthalpy, $\tilde{h}$, and mixture fraction, $\tilde{Z}$, are:

$$\frac{\partial \bar{\rho}}{\partial t} + \frac{\partial \bar{\rho}\tilde{u}_i}{\partial x_i} = 0 \tag{1}$$

$$\frac{\partial \bar{\rho}\tilde{u}_j}{\partial t} + \frac{\partial \bar{\rho}\tilde{u}_i\tilde{u}_j}{\partial x_i} = -\frac{\partial \bar{p}}{\partial x_j} + \frac{\partial}{\partial x_i}\left((\tilde{\mu}+\mu_t)\tilde{S}_{ij}\right) + (\bar{\rho}-\rho_\infty)g_j \tag{2}$$

$$\frac{\partial \bar{\rho}\tilde{Z}}{\partial t} + \frac{\partial \bar{\rho}\tilde{u}_i\tilde{Z}}{\partial x_i} = \frac{\partial}{\partial x_i}\left(\bar{\rho}(\tilde{D}+D_t)\frac{\partial \tilde{Z}}{\partial x_i}\right) \tag{3}$$

$$\frac{\partial \bar{\rho}\tilde{h}}{\partial t} + \frac{\partial \bar{\rho}\tilde{u}_i\tilde{h}}{\partial x_i} = \frac{\partial}{\partial x_i}\left(\bar{\rho}(\tilde{D}+D_t)\frac{\partial \tilde{h}}{\partial x_i}\right) - \overline{\nabla\cdot\dot{q}''_R} \tag{4}$$

The SGS contribution to the momentum stress and scalar flux is computed using a dynamic Smagorinsky model and a dynamic eddy diffusivity model, respectively [37]:

$$\tau^{sgs}_{u_iu_j} = -\bar{\rho}(\widetilde{u_iu_j} - \tilde{u}_i\tilde{u}_j) \approx 2\mu_t\tilde{S}_{ij} \tag{5}$$

$$\tau^{sgs}_{u_iZ} = -\bar{\rho}(\widetilde{u_iZ} - \tilde{u}_i\tilde{Z}) \approx \bar{\rho}D_t\frac{\partial \tilde{Z}}{\partial x_i} \tag{6}$$

where $\mu_t = C_s\bar{\rho}\Delta^2|\tilde{S}|$ is the turbulent eddy viscosity and $\bar{\rho}D_t = C_z\bar{\rho}\Delta^2|\tilde{S}|$ is the SGS diffusivity, with $|\tilde{S}| = \sqrt{2\tilde{S}_{ij}\tilde{S}_{ij}}$ being the norm of the resolved

strain rate tensor, $\tilde{S}_{ij}$, and Δ the filter width. Here, we take the filter width Δ equal to the grid-spacing. The coefficients C_s and C_z are calculated using dynamic procedures according to Refs. [37, 38].

The thermochemical variables, such as density, ρ, molecular diffusivity, D, and viscosity, μ, are provided by the combustion model described in the next section.

2.2. Combustion model

The combustion model is based on the non-adiabatic SLF model which parametrizes the local thermochemical state by the mixture fraction, Z, the scalar dissipation rate, χ, and the enthalpy defect, $X_R = h - h_{ad}$, where h_{ad} is the adiabatic enthalpy [39]. The SLF model relies on the underlying assumption that the thermophysical state of a particular flamelet relaxes to the steady-state solution on a sufficiently fast time-scale. However, radiative heat-loss processes evolve on time-scales that are slow compared to other processes in typical combustion applications [40, 41]. Based on this observation, several extensions of the SLF have been proposed [39, 40] to incorporate the radiative loss. On the other hand, Xu et al. [41] developed an unsteady flamelet model to couple combustion and radiation in a turbulent line fire. In the present study, the methodology described by Carbonell et al. [39] was used to incorporate radiative loss in the flamelet library. The idea consists in generating flamelet profiles for each strain rate with different degrees of heat losses. In practice, a volumetric radiative heat sink term based on the optically-thin approximation was introduced in the flamelet energy equation and was multiplied by a constant δ to allow variation in the degrees of radiative loss. For each strain rate, the flamelet temperature and species equations

were solved for a set of prescribed δ factors ranging from 0 (adiabatic) to the maximum value which was adjusted to be near quenching conditions. The flamelet library was generated by solving the governing equations of counterflow diffusion flames in physical space at a series of specified strain rates using the CHEMKIN code [42]. The mixture fraction distributions are obtained by solving a transport equation for the mixture fraction, as suggested by Pitsch and Peters [43]. The full chemical kinetic scheme developed by Li et al. [44] was used. Subgrid fluctuations of the combustion variables can have an important impact on the filtered properties due to the sensitivity and non-linearity of combustion processes. To account for subgrid fluctuations in the combustion variables, filtered combustion variables are obtained by integrating the flamelet library over the joint FDF of Z, χ and X_R.

$$\tilde{\phi} = \int \phi^{fl}(Z, \chi, X_R) \tilde{P}(Z, \chi, X_R) dZ d\chi dX_R \tag{7}$$

where the superscript fl refers to the flamelet library. Z, χ and X_R are assumed to be statistically independent and the marginal FDFs are modelled by a β-distribution for Z and δ-distributions for χ and X_R:

$$\tilde{P}(Z, \chi, X_R) = \beta(Z; \tilde{Z}, V_Z) \delta(\chi - \tilde{\chi}) \delta(X_R - \tilde{X}_R) \tag{8}$$

where V_Z is the SGS mixture fraction variance. The statistical independence between mixture fraction, scalar dissipation rate and enthalpy defect as well delta-Dirac FDF for scalar dissipation rate and enthalpy defect are commonly assumed in SLF/presumed PDF modelling [45]. The present model with these approximations was also applied in LES of a 0.5 m ethanol pool fire [46] and was found to provide an accurate description of the fire plume

structure. Once the flamelet library is computed and assumed FDF inte-grals are evaluated, a look-up table can be generated to provide the filtered thermochemical variables, consisting of temperature, density, molecular viscosity and diffusivity, and species mass fractions as functions of the quantities readily available from LES ($\tilde{Z}, V_Z, \tilde{\chi}$, and $\tilde{X}_R$) [47].

2.3. Subgrid scalar variance and dissipation modelling

The subgrid scalar variance, V_Z, required to retrieve solutions from the filtered flamelet look-up table, is defined in terms of a FDF as [48] :

$$V_Z(\mathbf{x}, t) = \widetilde{Z^2}(\mathbf{x}, t) - \tilde{Z}^2(\mathbf{x}, t) \tag{9}$$

where the appearance of the second moment $\widetilde{Z^2}$ makes the variance unclosed. In this work, we consider a transport equation for the second moment of the mixture fraction $\widetilde{Z^2}$ (STE) with the subgrid variance being then calculated from its definition, Eq. (9) :

$$\frac{\partial \bar{\rho}\widetilde{Z^2}}{\partial t} + \frac{\partial \bar{\rho}\tilde{u}_i\widetilde{Z^2}}{\partial x_i} = \frac{\partial}{\partial x_i}\left(\bar{\rho}(\tilde{D} + D_t)\frac{\partial \widetilde{Z^2}}{\partial x_i}\right) - \bar{\rho}\tilde{\chi} \tag{10}$$

The remaining modelling step for STE concerns the filtered scalar dissipation rate, $\tilde{\chi}$. Jiménez et al. [48] proposed to model the filtered scalar dissipation rate by relating the SGS scalar mixing time scale to the SGS turbulent time scale. An equivalent SGS turbulent characteristic time $\bar{\tau}$ is introduced as the ratio between SGS kinetic energy, $\kappa^{sgs} = 1/2(\widetilde{u_i u_i} - \tilde{u}_i\tilde{u}_i)$, and the filtered kinetic energy dissipation rate, $\tilde{\varepsilon} = \tilde{\nu}\widetilde{\frac{\partial u_i}{\partial x_j}\frac{\partial u_i}{\partial x_j}}$. Given a proportionality between both time scales, the model for $\tilde{\chi}$ is derived as:

$$\frac{\tilde{\chi}}{V_Z} = \frac{1}{\tilde{\tau}_Z} \approx \frac{C}{\tilde{\tau}} = C\frac{\tilde{\varepsilon}}{\kappa^{sgs}} \tag{11}$$

Therefore, the filtered scalar dissipation rate, $\tilde{\chi}$, can be written as [48] with C_I computed by dynamic approach:

$$\tilde{\chi} = \frac{\tilde{D} + D_t}{C_I \Delta^2} V_Z \tag{12}$$

2.4. Radiation modelling

The spectral coverage range in terms of wavenumber, η, is 0-25000 cm^{-1} and H_2O and CO_2 are considered as the only radiating species since the contribution of CO can be neglected. The RCFSK is used as gas radiative property model [49]. As in the classical FSK [50], the FS cumulative k-g distribution function, is defined as $g(k, \phi, T_p) = \int_0^\infty H[k - \kappa_\eta(\phi)] I_{b\eta}(T_p) d\eta / I_b(T_p)$, where H is the Heaviside function, κ_η is the spectral absorption coefficient, $\phi = \{x_{CO_2}, x_{H_2O}, T\}$ is an array of thermodynamic variables affecting κ_η. x_{CO_2} and x_{H_2O} represent the mole fractions of CO_2 and H_2O, respectively. $I_{b\eta}$ and I_b are the spectral and total blackbody intensities at the blackbody temperature, T_p, respectively. The main advantage of the RCFSK is that it does not require any specification of a reference state [50]. Mixed FS k-g distributions (for mixtures of H_2O and CO_2) are constructed from HITEMP 2010 [51] by using the procedure proposed by Modest and Riazzi [50]. The FSK RTE can be written as:

$$\frac{dI_{g_0}}{ds} = -k^*(g_0) I_{g_0} + k^*(g_0) a(g_0) I_b(T_p) \tag{13}$$

where g_0 corresponds in the present study to a quadrature-point of a 10-point Gauss-Legendre quadrature scheme and I_{g_0} is the radiative intensity at this quadrature point [49]. The RCFSK scheme determines the absorption coefficient by solving $g(k^*, \phi, T_p) = g_0$ whereas the stretching function is

computed as $a = \partial g[k(g_0, \phi, T_p), \phi, T]/\partial g_0$ [49]. The total radiative intensity, I, and the total incident radiation, G, are computed as $I = \int_0^1 I_{g_0} dg_0$ and $G = \int_{4\pi} I d\Omega$, respectively. The divergence of the radiative flux is then calculated from the following equation [52]:

$$\nabla \cdot \dot{q}''_R = \int_0^1 4\pi k^* a I_b dg_0 - \int_0^1 k^* G dg_0 \tag{14}$$

Predictions were found insensitive to the choice of T_p. In the present simulations, T_p was set equal to 1500 K.

The filtered RTE and divergence of the radiative flux are obtained by applying the filtering operation to Eqs. (13) and (14):

$$\frac{d\overline{I_{g_0}}}{ds} = -\overline{k^* I_{g_0}} + \overline{k^* a I_b} \tag{15}$$

$$\overline{\nabla \cdot \dot{q}''_R} = \int_0^1 4\pi \overline{k^* a I_b} dg_0 - \int_0^1 \overline{k^* G} dg_0 \tag{16}$$

The filtered absorption terms, $\overline{k^* I_{g_0}}$ or $\overline{k^* G}$, are closed by neglecting the SGS absorption, leading to $\overline{k^* I_{g_0}} \approx \overline{k^*}\ \overline{I_{g_0}}$ and $\overline{k^* G} \approx \overline{k^*}\ \overline{G}$. The filtered absorption coefficient and emission terms are closed by using the presumed FDF approach:

$$\overline{k^*} = \bar{\rho} \int \frac{(k^*)^{fl}(Z, \tilde{\chi}, \tilde{\chi}_R)}{\rho^{fl}(Z, \tilde{\chi}, \tilde{\chi}_R)} \beta(Z; \tilde{Z}, V_Z) dZ \tag{17}$$

$$\overline{k^* a I_b} = \bar{\rho} \int \frac{(k^* a I_b)^{fl}(Z, \tilde{\chi}, \tilde{\chi}_R)}{\rho^{fl}(Z, \tilde{\chi}, \tilde{\chi}_R)} \beta(Z; \tilde{Z}, V_Z) dZ \tag{18}$$

The Filtered RTE is solved by using FVM with an angular mesh of $N_\theta \times N_\phi = 16 \times 24$ control angles [52]. N_θ and N_ϕ represent the polar and azimuthal angles, respectively.

2.5. Numerical solution

The Favre-filtered transport equations are solved by using the second-order iterative variable-density pressure-based low-Mach number solver developed by Ma et al. [53] and implemented in the finite volume code *Code_Saturne* v5.0.9 [54], employing cell-centered collocated grids. The second-order Crank-Nicolson scheme is used for time advancement. For scalar transport, numerical oscillations must be prevented through non-oscillatory schemes. We employ a Total Variation Diminuishing (TVD) scheme that blends a second order central scheme with a first order upwind scheme in a way that combines good accuracy with limited numerical oscillation. Avoiding numerical oscillation is particularly important for reacting scalars (here the mixture fraction), as the density depends on them in a strongly non-linear manner. A second-order central difference scheme (CDS) is used for diffusion. For the momentum equation both convective and diffusive terms are also discretized by using a second-order CDS. Numerical details and a method of manufactured solutions (MMS) verification of the predictor-corrector approach can be found in Ref. [53].

3. Results and discussions

3.1. Computational details

The baseline configuration is the 30.5 cm diameter methanol pool fire investigated experimentally by Weckman and Strong [12]. In these experiments, the methanol feed rate was maintained at 1.35 $cm^3.s^{-1}$. The corresponding heat release rate (HRR, $\dot{Q}$) is 22.45 kW. Weckman and Strong reported measurements of mean and rms velocity and temperature. Velocities were measured

by using a two-component laser Doppler anemometer with uncertainties of $\pm$ 5 % on mean values and $\pm$ 15 % on rms values. In addition, power spectral density (PSD) computed from time series of radial and axial velocities revealed a puffing frequency of 2.8 Hz. Temperatures were measured with 50 μm diameter bare-wire Pt-Pt/l0 % Rh thermocouples with bead diameters in the range of 75-100 μm. Temperature measurements were corrected to account for the thermal inertia of the thermocouple bead. The compensation technique was based on an instantaneous time constant computed from the thermocouple geometry and an estimation of the flow conditions for the convective heat transfer. The uncertainties on mean temperature were estimated to be $\pm$ 5 % whereas those on the rms values were found to be difficult to estimate mainly due to the uncertainty on the compensation method. However, uncertainties as high as 25-30 % were reported using thermocouples to obtain measurements of fluctuating temperature [8, 12, 55]. This set of experimental data is completed by those obtained by Hamins et al. [16], Hamins and Lock [17] and Kim et al. [18] who also considered 30 cm diameter methanol pool fires. Hamins et al. [16] measured the radiative feedback towards the fuel surface. Hamins and Lock [17] reported axial and radial distributions of mean temperature that were in good accordance with the measurements of Weckman and Strong [12]. They also reported axial distribution of species volume fractions. Kim et al. [18] measured radial (at the level of the burner rim) and axial (at a distance of 60 cm from the pool axis) distributions of radiative flux. In addition, they measured the local total heat flux in the downward direction at 3 mm above the fuel surface.

In the baseline case, consistently with the experimental configurations re-

ported in Refs. [12, 17, 18], the burner stands at one-pool diameter above the floor and fuel lip height is set equal to 1 cm (see Fig. 1a). Two other configurations are considered by modifying the burner boundary conditions while keeping the pool diameter and HRR unchanged. In order to investigate the effects of the fuel lip height on the pool fire dynamics, the first configuration, referred to as NoLip hereafter, considers the same configuration as the baseline case, except that the fuel level coincides now with the pan rim (see Fig. 1b). The second configuration, referred to as NoLipNoEnt hereafter, modifies the NoLip configuration by considering that the burner rim is now floor flush, altering thus the air entrainment at the pool basis (see Fig. 1c).

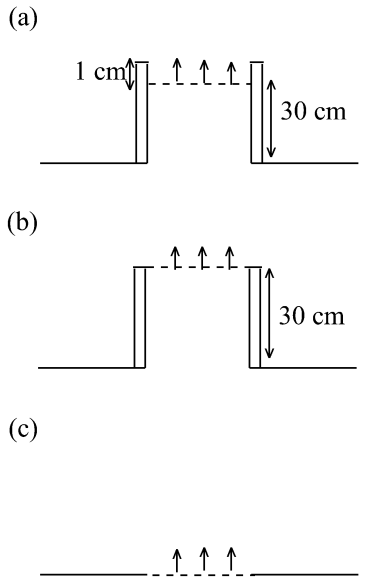

Figure 1: A shematic diagram of the three burner boundary conditions for the: (a) baseline case, (b) NoLip case, and (c) NoLipNoEnt case.

Simulations are performed in a computational domain (x, y, z) of $3 \times 3 \times 3$

m^3. The mesh is uniformly refined in the region of $0.4 \times 0.4 \times 0.1$ m^3 centered around the burner, with a minimal grid spacing equal to 2.5 mm. Outside this region, Δx and Δy are stretched progressively towards the sides of the computational domain. In the vertical direction, Δz is stretched from z = 0.1 m to z = 0.2 m to reach 5 mm. An uniform $\Delta z = 5$ mm is then applied up to z = 0.6 m. Above z = 0.6 m, Δz is stretched progressively.

The mean flame height was measured as 0.51 m [16]. Therefore, the grid resolution is lower than 5 mm in the flaming region and can be compared to estimations of the Kolmogorov length scale, η_k, and the Taylor length scale, λ. These estimations will be made by using the analysis proposed in Refs.[32, 56] at $z = 0.2$ m, which corresponds approximately to the continuous flame tip based on the axial temperature measurements of Weckman and Strong [12]. The integral length scale, L_t, is assumed to be one-half of the pool diameter [32, 56], leading to $L_t = 0.15$ m. The fluctuating axial velocity, w', and the temperature rise above the ambient, ΔT, at $z = 0.2$ m are about 1.07 $m.s^{-1}$ and 944 K [12], respectively. The kinematic viscosity is estimated from $\nu = \nu_\infty(1 + \Delta T/T_\infty)^{1.7} = 173 \times 10^{-6} m^2.s^{-1}$ [56] where $\nu_\infty = 15 \times 10^{-6} m^2.s^{-1}$ is the kinematic viscosity at the ambient temperature, $T_\infty = 293$ K. This leads to a turbulent Reynolds number of $Re_t = w' L_t/\nu = 925$, and, in turn, to a Kolmogorov length scale, $\eta_k = L_t Re_t^{-3/4}$, of about 0.9 mm. The Taylor length scale can then be deduced from $\lambda = \sqrt{10} L_t Re_t^{-1/2} \approx 15.5$ mm [57]. This analysis shows that the present LES are resolved well beyond the Taylor microscale and that the filter size is about 6 times the Kolmogorov length scale.

Concerning the boundary conditions, typical outflow/inflow boundary con-

ditions are used for open boundaries at the sides. At the inlet, a spatially uniform and steady inlet velocity is imposed to provide the specified HRR and both convective and diffusive mass and energy fluxes are accounted for. The inlet temperature is set to the boiling point of methanol, i.e. 338 K. At the domain exit, a convective condition is used. In the rest of the domain, the classical wall boundary condition is imposed.

Throughout all simulations, the time step is set to 5×10^{-4} s which corresponds to an averaged maximum CFL of 0.6. Simulations were run for 25 s and the time-averaged mean and rms values were collected over the last 19 s. The first 6 s of simulation were used to establish a statistically stationary flow.

3.2. Quality of LES

The ratio of resolved temperature variance, $\sigma_{T,ReS} = \langle \tilde{T}^2 \rangle - \langle \tilde{T} \rangle^2$, to the total temperature variance, $\sigma_T = \widetilde{\langle T^2 \rangle} - \langle \tilde{T} \rangle^2$, is considered to assess the quality of the present LES. Figure 2 shows radial profiles of this ratio at different heights above the burner covering the flaming region. It can be observed that more than 80 % of temperature variance is on the whole resolved by the present LES.

3.3. Comparison with available experimental data

Model predictions for the baseline case are compared to the available experimental data.

The predicted puffing frequency of 2.37 Hz was estimated from a Fast Fourier Transform of the time series of the axial velocity along the axis at z = 0.2 m. This location was selected because the corresponding experimental PSD

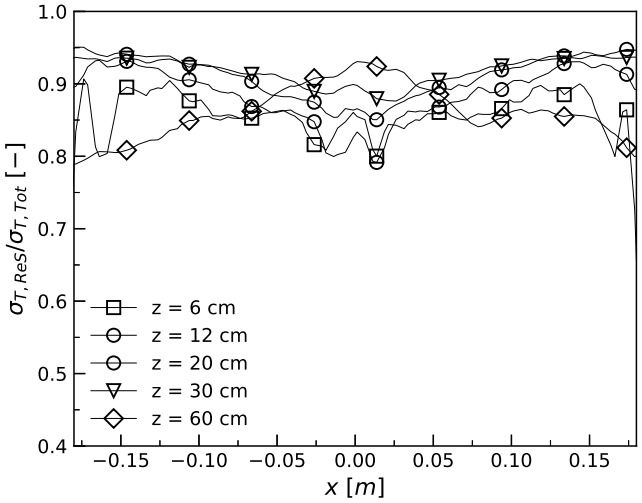

Figure 2: Radial evolution of resolved part of temperature variance at different heights.

was found to exhibit a distinct puffing frequency [12]. This computed puffing frequency underestimates the experimental one of 2.80 Hz by about 18%. Figure 3 shows the mean temperature as a function of the normalized height, $(z^* = z/\dot{Q}^{2/5})$, defined by McCaffrey [4]. Experimental data shows that the axial temperature increases with z^* up to $z^* \approx 0.02\ m.kW^{-2/5}$, reaches a plateau of about 1300 K between $z^* \approx 0.02\ m.kW^{-2/5}$ and $z^* \approx 0.04\ m.kW^{-2/5}$, and decreases as z^* is further increased. The model reproduces well the temperature peak as well as the experimental profile for $z^* \geq 0.03\ m.kW^{-2/5}$. For lower z^*, the axial temperature is underpredicted although it is in overall within the measurement uncertainty of Hamins and Lock [17].

Figures 4 to 9 display the radial profiles of mean and rms temperature, axial velocity and radial velocity at different heights. Model predictions present

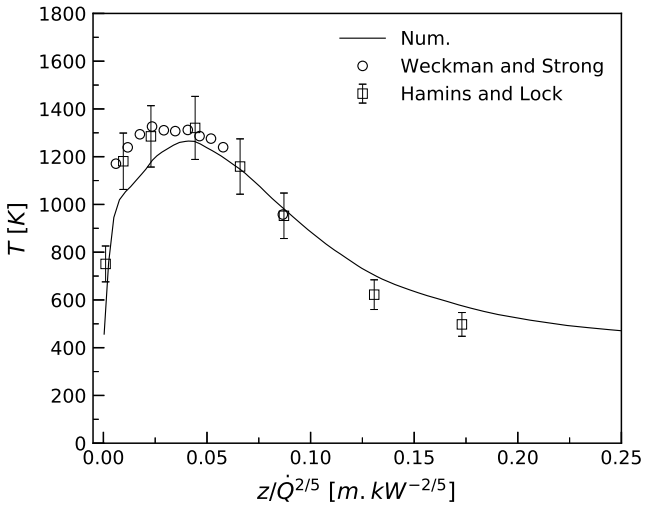

Figure 3: Axial profile of mean temperature. The experimental data are taken from Refs. [12, 17].

an overall good agreement with the experimental data. In particular, the simulations capture well the radial spreading of the fire plume. The profiles of mean temperature are on the whole well reproduced by the model at all the heights (see Fig. 4). However, in the lower part of the fire plume ($z \leq 10$ cm), the predicted mean temperature exhibits M-shaped profiles that are not observed experimentally (see Fig. 4). This results in an underestimation of the centreline temperature in this region as discussed previously. Measurements of temperature by 50 μm thermocouples may lead to a significant underestimation of temperature fluctuations despite the use of compensation technique [8, 12, 55]. Consequently, the overprediction of the temperature fluctuations by the model observed in Fig. 5 is not surprising. However, Fig. 5 shows that the predicted temperature fluctuations follow the same trends as the experiments.

Figures 6 and 7 show that the radial profiles of mean axial velocity and rms values of axial velocity fluctuations exhibit an overall good agreement with the experimental data. However, close to the pool surface (z = 2 and z = 4 cm), the predicted axial velocity exhibits a M-shaped profile that is not observed experimentally and overestimates the measurements along the flame wings (see Fig. 6). On the other hand, axial velocity fluctuations are slightly overpredicted for $z > 14$ cm (see Fig. 7).

Figures 8 and 9 show that the comparison is less satisfactory for radial velocity statistics than for axial velocity statistics. A careful examination of Fig. 8 shows that the experimental profiles of mean radial velocity are not symmetric with respect to the fire plume axis and that the values at the centreline are not equal to zero. This dissymmetry, although less pronounced, is also observed for the radial velocity fluctuation at some heights (see Fig. 9) and reflects the difficulty to make accurate measurements of radial ve-locity, especially at vicinity to the flame axis. Figure 8 shows a reasonable agreement with measurements in the wings of the profiles for $z > 8$ cm de-spite an overall 10 % underprediction. For $z \leq 8$ cm, larger discrepancies are observed. At these heights, the experimental maximum value (in abso-lute), observed at about x = 10 cm, is significantly underestimated and its predicted location is shifted away from the plume axis as compared to the measurements.

Concerning the radial profiles of rms radial velocity, a good accordance between simulations and measurements is observed at the tails of the profiles (see Fig. 9). Nevertheless, the computed fluctuations exhibit well pronounced M-shaped profiles whereas the measured ones are flatter, which results in an underestimation of the fluctuations of radial velocity close to

the centerline.

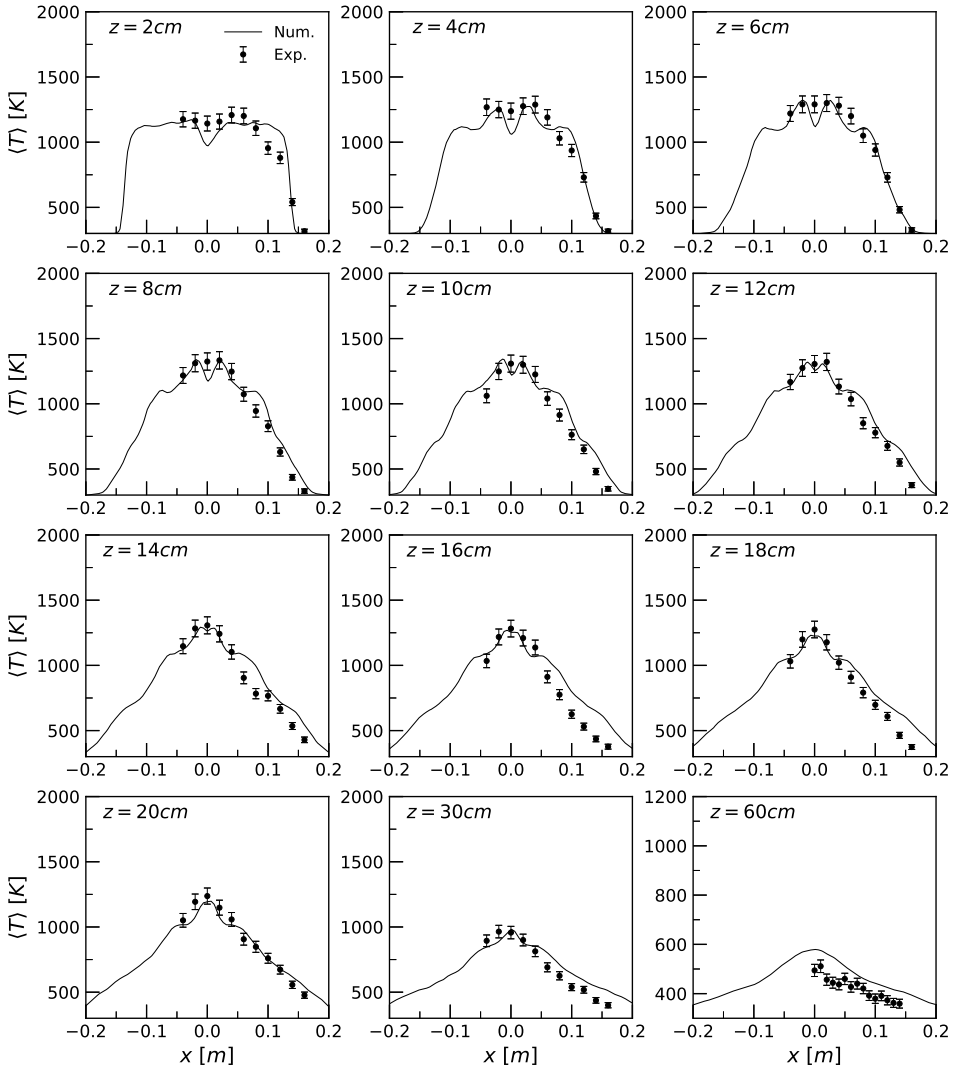

Figure 4: Radial profiles of mean temperature at different heights. The experimental data are taken from Ref. [12], except the radial profile at z=0.6 m that is taken from Ref. [17].

Figure 10 shows the axial profiles of the molar fractions of CH_3OH, O_2, CO_2, H_2O, CO and H_2. The model reproduces quantitatively the experimental

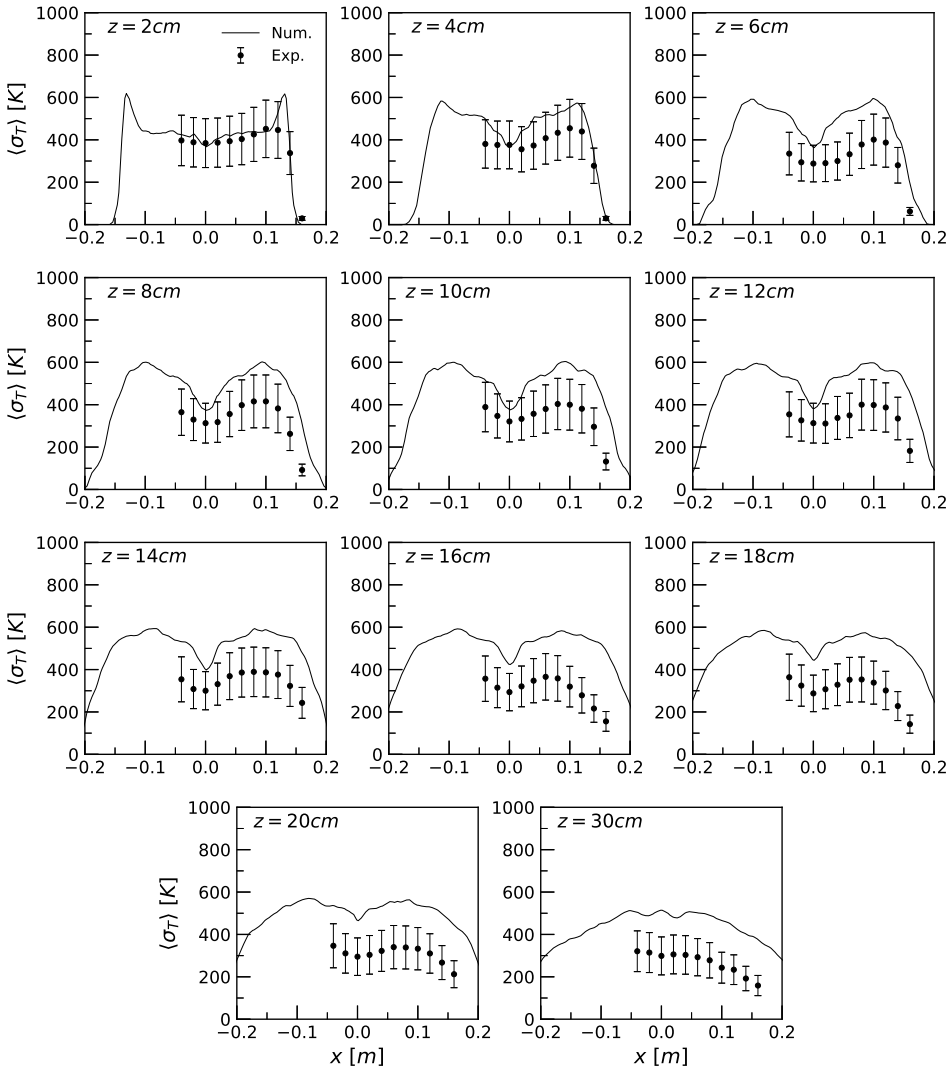

Figure 5: Radial profiles of rms value of temperature at different heights. The experimental data are taken from Ref. [12].

data for CH_3OH, O_2, CO_2, CO and H_2. The rapid decrease in the mole fraction of CH_3OH as well as the depletion of O_2 in the flaming zone are well predicted. The profiles of mole fractions of CO, CO_2, and H_2 are also

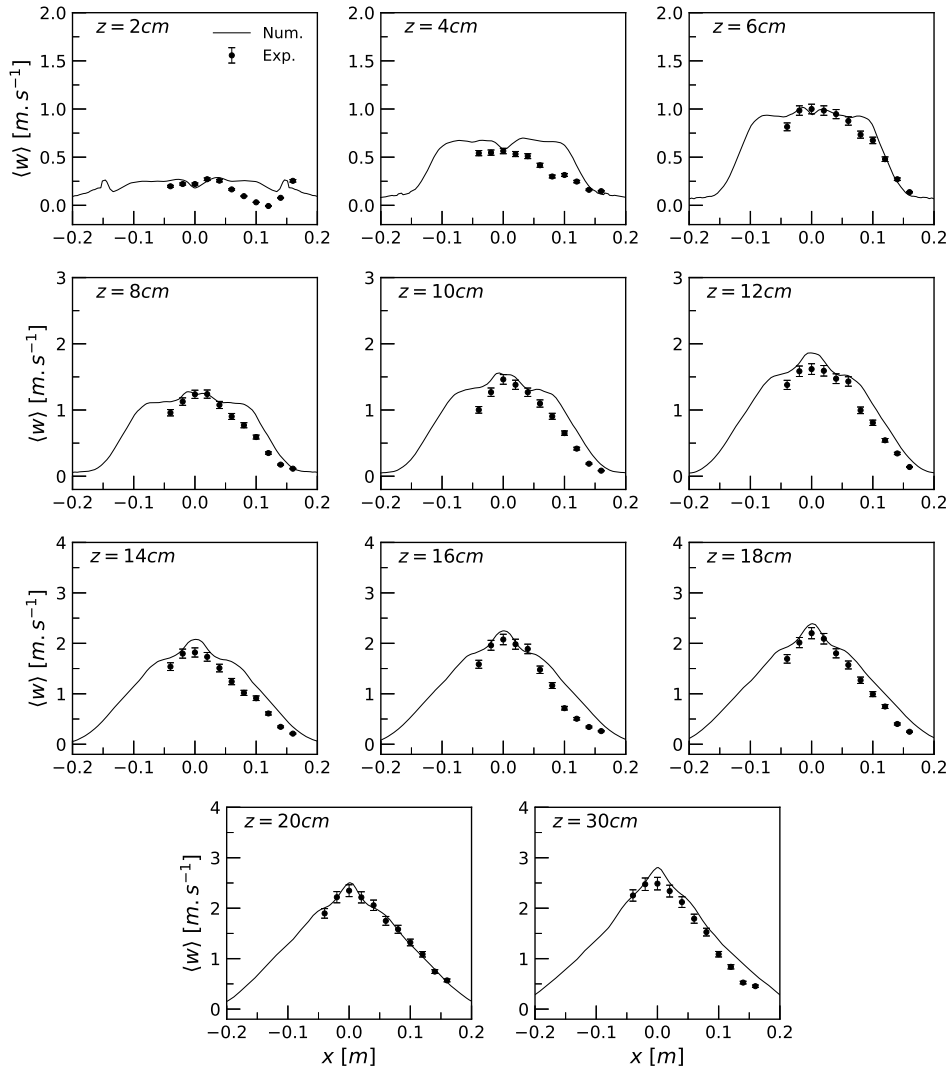

Figure 6: Radial profiles of mean axial velocity at different heights. The experimental data are taken from Ref. [12].

in good agreement with the experiments although the peak of CO mole fraction is overestimated. Finally, the model underestimates significantly the H_2O molar fraction over the entire fire plume axis. Surprisingly, such large

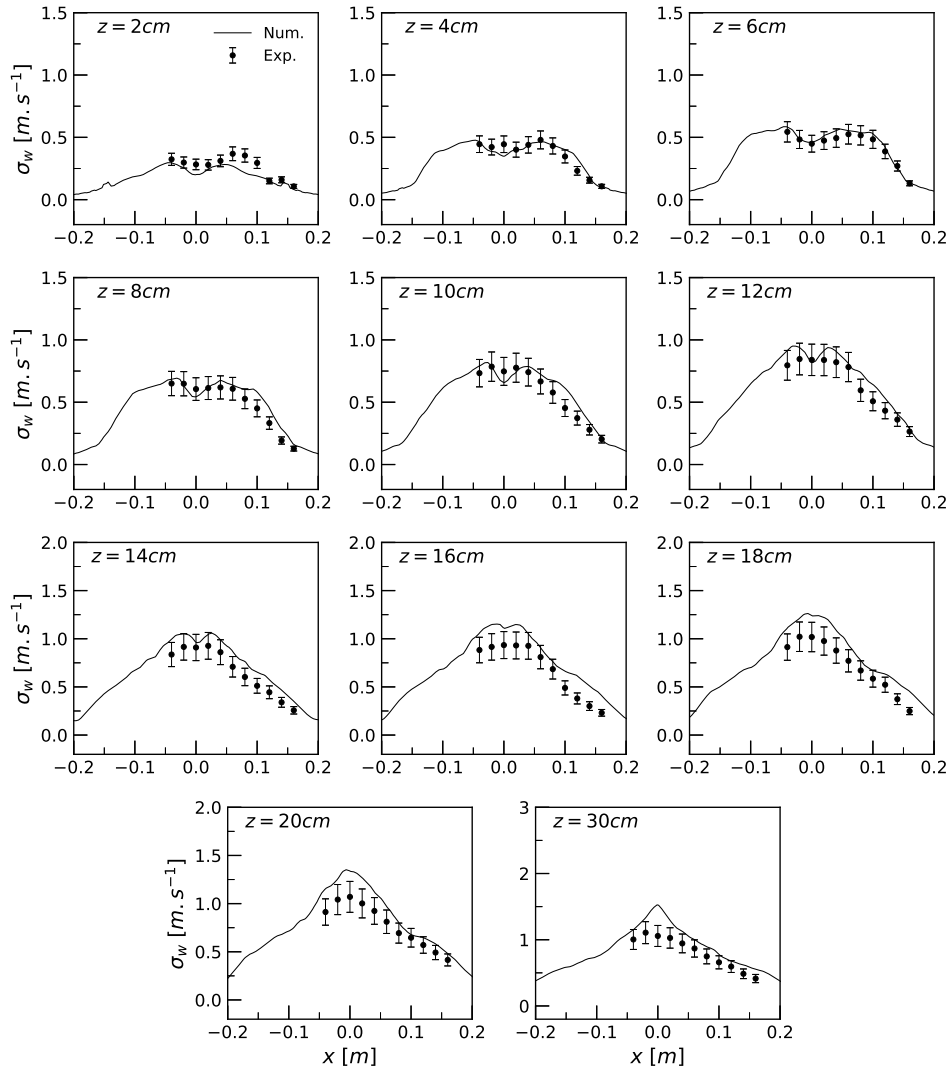

Figure 7: Radial profiles of rms value of axial velocity at different heights. The experimental data are taken from Ref. [12].

discrepancies are only observed for H_2O whereas, as discussed previously, a rather good agreement is observed for the other species. An examination of the error bars reported by Hamins and Lock [17] (see Fig. 10) shows that

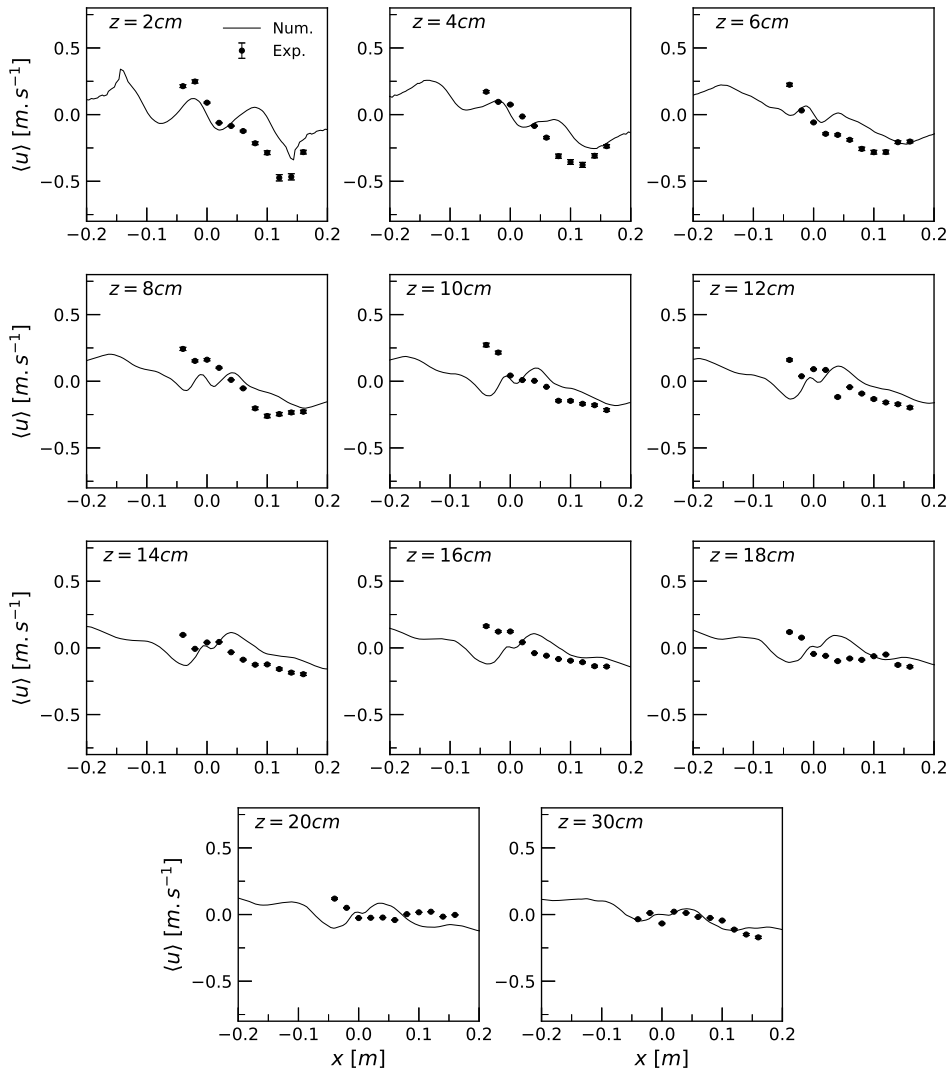

Figure 8: Radial profiles of mean radial velocity at different heights. The experimental data are taken from Ref. [12].

the experimental uncertainties associated to the measurements of H_2O are significantly higher than for the other species. This can explain, at least partially, these large discrepancies.

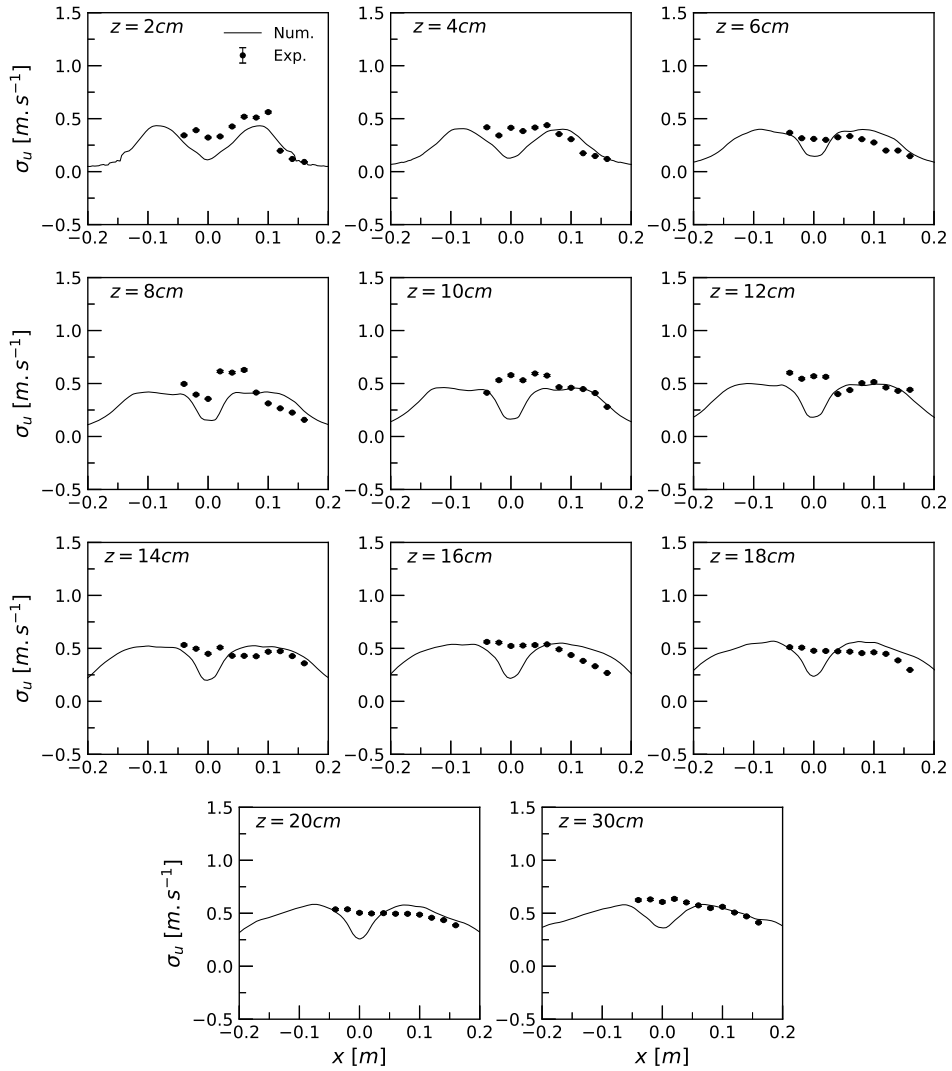

Figure 9: Radial profiles of rms value of radial velocity at different heights. The experimental data are taken from Ref. [12].

The radiant fraction is computed by integrating the time-averaged divergence of the radiative flux over the computational domain, $\chi_R = \int \nabla \cdot \dot{q}''_R dV/\dot{Q}$. The predicted radiant fraction is 0.261 and overestimates the measured one

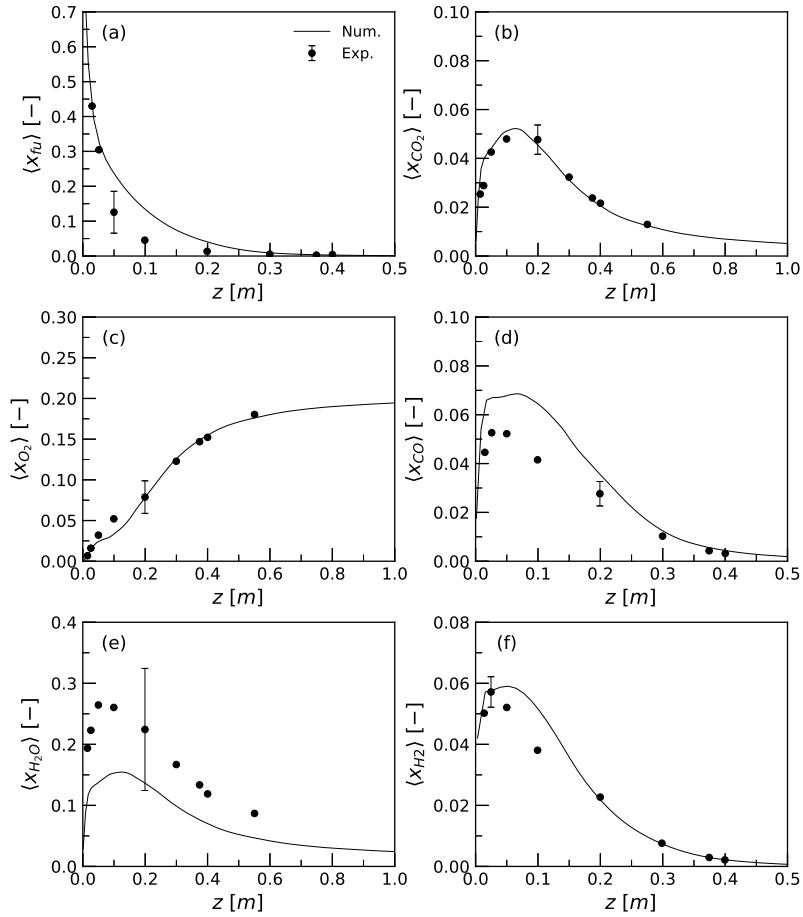

Figure 10: Axial profiles of mean molar fractions for: a) methanol, b) carbon dioxide, c) oxygen, d) carbon monoxide, e) water vapor and f) hydrogen. The experimental data are taken from Ref. [17].

of 0.24 ± 25 % by about 8.75 %. Figure 11a shows the vertical distribution of radiative flux at a distance of 0.6 m from the fire plume axis. The distribution exhibits ray effects when computed with the 16 × 24 angular mesh. A frozen field radiative calculation was performed with a finer angular mesh with 48 × 96 control angles in order to improve this behavior and the

corresponding prediction is plotted in Fig. 11a.

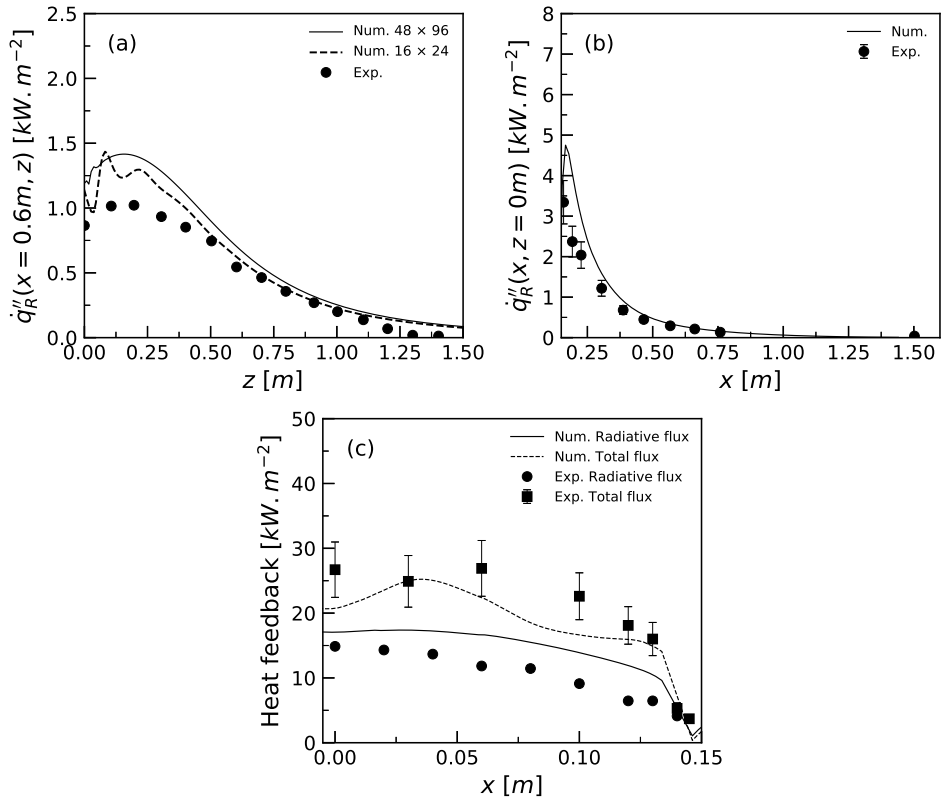

Figure 11: Heat fluxes: (a) Vertical distribution of radiative flux at a distance r = 0.6 m from the pool axis, (b) radial distribution of the radiative heat flux in the downward direction outside the burner, and (c) radiative and total heat feedback to the fuel surface. The experimental data are taken from Ref. [18], except those for the radiative feedback that are taken from Ref. [16].

In this calculation, instantaneous fields of absorption coefficient and emission term, computed with the 16 × 24 angular mesh, are saved during the statistically stationary state. These fields are used to solve the instantaneous RTE with the finer angular mesh and, subsequently compute the time-averaged

radiative outputs. This approach is justified by the fact that the finer mesh was found to have no influence on the prediction of the radiative heat transfer inside the flame and to change only the radiative flux outside the flame. These observations are in line with those reported by Jensen et al. [58] who showed that radiative outputs within the flame, where radiation is isotropic, can be accurately computed with a coarse angular discretisation whereas a finer one is required to avoid ray effects on radiative flux outside the flame. Figure 11a shows that the model overestimates the radiative flux, especially for $0 \leq z \leq 0.5$ m. A better agreement is observed downstream.

Figure 11b shows the radial distribution outside the burner along the plane of the burner rim. Predictions, obtained with the 16×24 angular mesh, are in overall good agreement with the experimental data. Nevertheless, the model overpredicts the radiative flux at vicinity of the burner. Figure 11c shows both radiative and total heat feedback to the fuel surface. The reported fluxes were also computed with the 16×24 angular mesh. As dis-cussed by Hamins et al. [16], the experimental radiative feedback decreases continuously from the center towards the edge. This continuous decrease is also observed for the simulations although it is less pronounced. In addi-tion, the model overestimates the experimental data. The model ignores the radiative contribution of the methanol whose the importance for estimating the radiative feedback is recognized [59]. This can explain at least partially the discrepancies between the model and the experiments. Another source of discrepancies may be attributed to the difference in fuel lip heights be-tween the simulations and the experiments. The simulations considered a fuel lip height of 1 cm whereas that reported by Hamins et al. [16] was 0.5

cm. Figure 11c compares the predicted total heat feedback at the fuel sur-face with that measured by Kim et al. [18]. The experimental heat flux is approximately constant for $x < 6$ cm with a value around 26 $kW.m^{-2}$ and, then, decreases with distance towards the pool edge to reach 16 $kW.m^{-2}$ at $x = 13$ cm. As the distance towards the pool edge is further increased, a very sharp decrease of the total heat flux is observed to reach 3.7 $kW.m^{-2}$ at $x = 14.5$ cm. The model reproduces correctly this behavior. Nevertheless, the computed total heat flux underestimates in overall the measurements with a maximum deviation of about 20% at $x = 10$ cm.

3.4. Pool boundary condition effects

This section analyses the differences induced by the different burner boundary conditions on the fire plume structure. These differences can be attributed to effects on the formation and growth of the flame base non-dissipative laminar instability near the edge of the pool that develops periodically to form energy containing large-scale toroidal vortices [60]. These vortices govern the flow pattern, the air entrainment as well as the mixing and combustion processes [61–63]. Once generated near the edge of the source due to baroclinic and gravitational torques, these vortices convect upward and act like a pump, inducing the necking-in behavior at the base of the flame b eneath them where air is engulfed. Figures 12, 13, and 14 show sequences of snapshots of temperature in the centreline (x-z) plane for the baseline case, the NoLip case and the NoLipNoEnt case, respectively. On each figure, t he t ime step between two snapshots is 0.06 s. In these figures, t he a rrows i ndicate the directions of the density gradients, $\nabla\rho$, the pressure gradient, ∇p, and the gravity, $\mathbf{g}$. These snapshots are supplemented by, on the one hand, time-

averaged axial and radial profiles at different heights of mean temperature and axial velocity (see Fig. 15) and, on the other hand, radial distributions of rms values of temperature and axial velocity (see Fig. 16).

Let us start to describe the sequence for the baseline case (see Fig. 12). Figure 12a shows a coherent structure in the middle of the image. On the other hand, the flame is anchored on the top of the burner rim in accordance with the experimental observations made by Weckman and Sobiesiak [10]. The air entrained at the pool basis bypasses the rim and leads to a wrinkling of the flame sheet. This wrinkled flame sheet is subjected to a Rayleigh-Taylor instability as illustrated in Fig. 12b. This results in the formation of a raising hot "bubble" structure whereas the air flows towards the fuel surface as evidenced in Fig. 12c. The growth of the hot structure results in another unstable configuration (see Fig. 12d), which produces buoyant and baroclinic vorticity generation. In Fig. 12e, the resulting vortex sheet begins to roll up into what will become the next coherent turbulent structure. The growth of this coherent structure and the characteristic necking behavior beneath it are illustrated in Fig. 12f to h. Figure 13 shows a similar sequence for the NoLip configuration. The flame is anchored to the burner edge (see Fig. 13a). Contrary to the baseline configuration, no wrinkling of the flame sheet is observed near the edge of the pan and the misalignment between, on the one-hand, the density gradient and, on the other hand, gravity and pressure gradient, although still presents, is lower than for the baseline case (see Figs. 13a and b). As a result, the formation of the hot "bubble" structure as described for the baseline case is not observed although Fig. 13c shows the appearance of smaller instabilities. As for the baseline case, the growth of

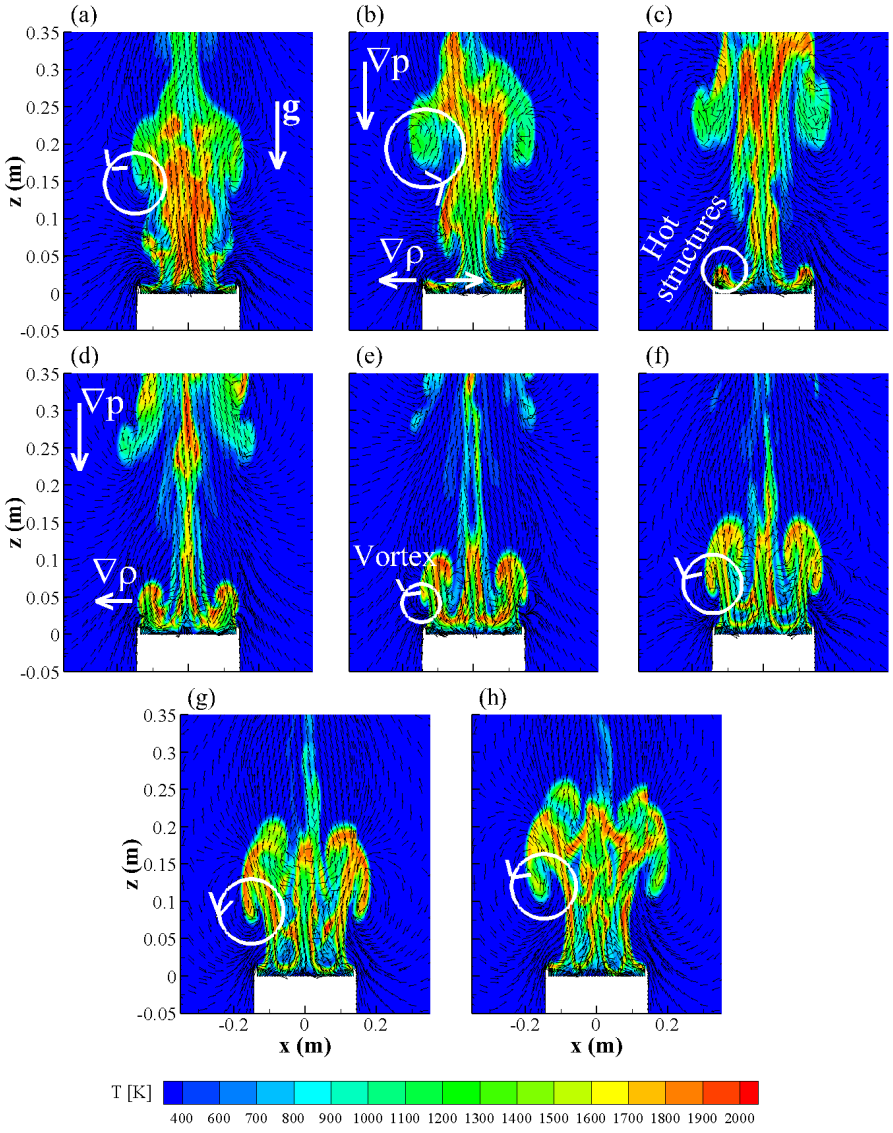

Figure 12: Snapshots of temperature at different times for the baseline case. The time between two snapshots is 0.06 s. Uniform velocity vectors are plotted to illustrate the flow pattern.

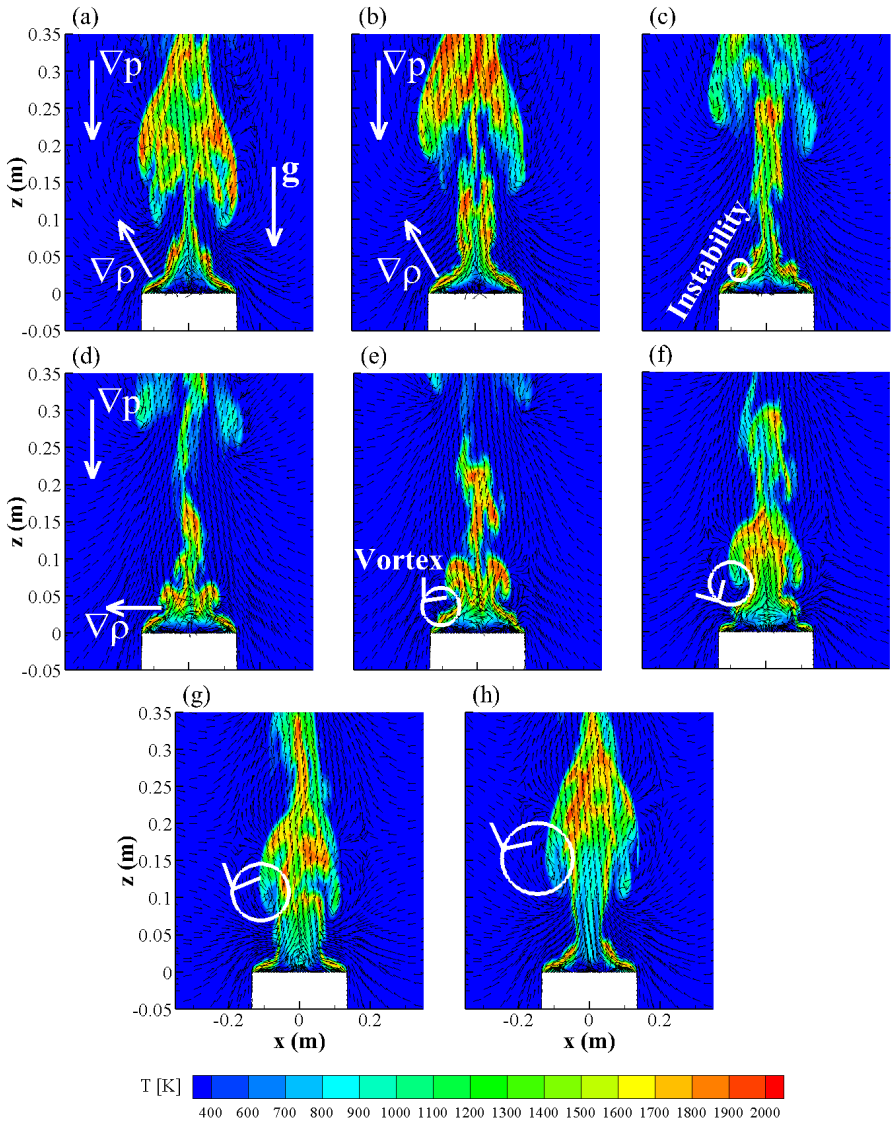

Figure 13: Snapshots of temperature at different times for the NoLip case. The time between two snapshots is 0.06 s. Uniform velocity vectors are plotted to illustrate the flow pattern.

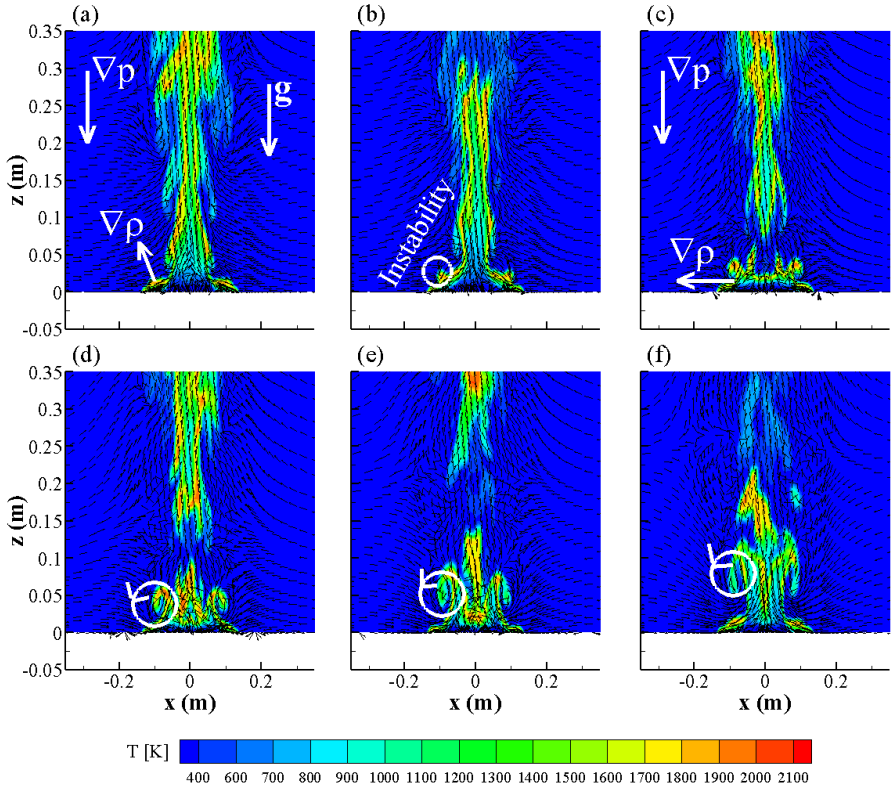

Figure 14: Snapshots of temperature at different times for the NoLipNoEnt case. The time between two snapshots is 0.06 s. Uniform velocity vectors are plotted to illustrate the flow pattern.

this instability results in an unstable configuration (see Fig. 13d) and in the generation of a vortex that develops as it is convected upward (see Figs. 13e to h).

This comparison illustrates the significant effects of the fuel lip height on the formation of instabilities. The inclusion of the fuel lip height modifies considerably the flow pattern due to the formation of hot "bubble" structures stemming from the interactions between the air entrainment at the pool ba-

sis, the burner rim and the flame sheet. These hot structures contribute to enhance significantly the mixing at vicinity of the burner as illustrated by the much wider fire plume (see Figs. 15 and 16) and the higher temperature and velocity fluctuations (see Figs. 16) observed when the fuel lip height is considered. In addition, Figs. 15b-d and f-h show that the fire plume close to the burner is hotter and raises at a higher velocity in presence of the fuel lip height. As described by Orloff and de Ris [34, 35] from their experiments, this enhanced mixing results in a shorter flame, as illustrated in Fig. 15a and e by the lower temperature and axial velocity observed along the axis in the intermittent flame region and in the inert plume ($z^* > 0.05\ m.kW^{-2/5}$). On the other hand, considering or not the fuel lip height has weak effect on the puffing frequency that is 2.27 Hz for the NoLip case instead of 2.37 Hz for the baseline case.

Comparing Figs. 13 and 14 shows that modifying the air entrainment at the base of the pool changes the flow pattern. In the case where the pool is located one-pool diameter above the floor (NoLip), the air entrained at the edge of the pan comes from both the sides and the bottom (see Fig. 13a) whereas, in the NoLipNoEnt case, the floor prevents the part coming from the bottom and air entrainment comes only from the sides (see Fig. 14a). This stronger lateral air entrainment in the NoLipNoEnt case has two effects. First, it pushes the flame sheet anchored to the pan edge towards the liquid surface and, as a result, reduces the misalignment between density gradient and both gravity and pressure gradient as compared to the NoLip case (see Figs. 13a and 14a). This reduces both gravitational and baroclinic

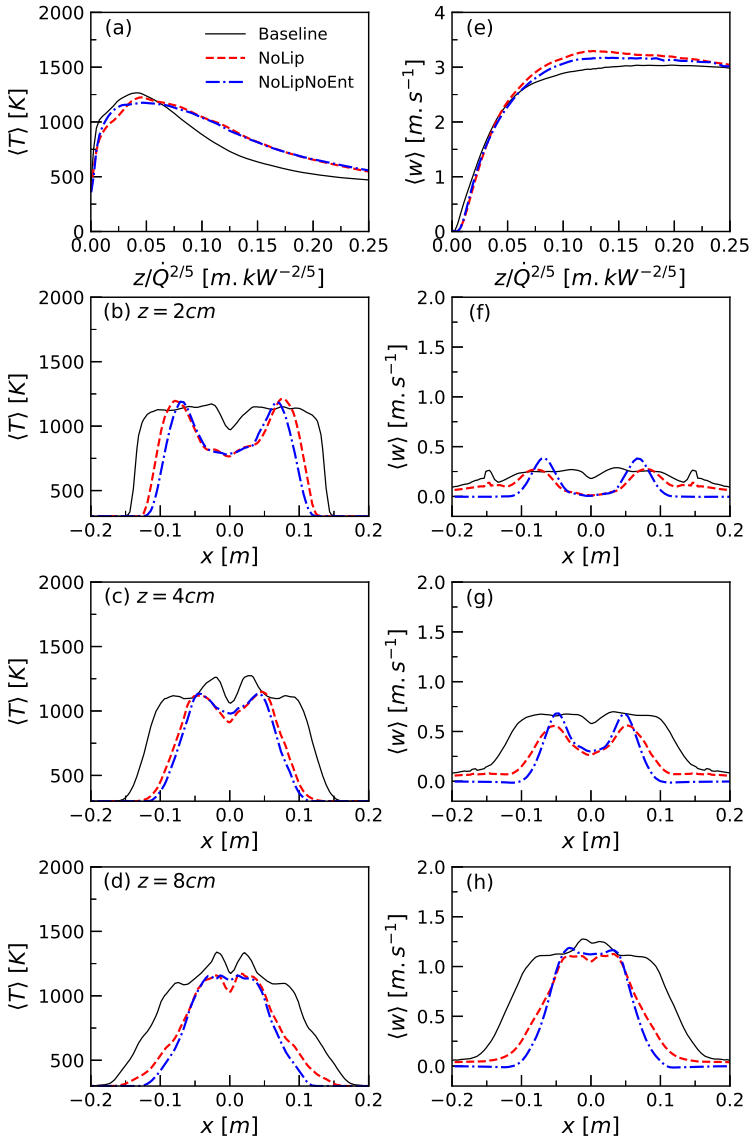

Figure 15: Effects of pool boundary conditions on axial and radial profiles at different heights of mean temperature and axial velocity.

torques and, in turn, the strength of the first instability. This is illustrated by comparing Figs. 13c and 14b. Second, the coherent vortices, generated

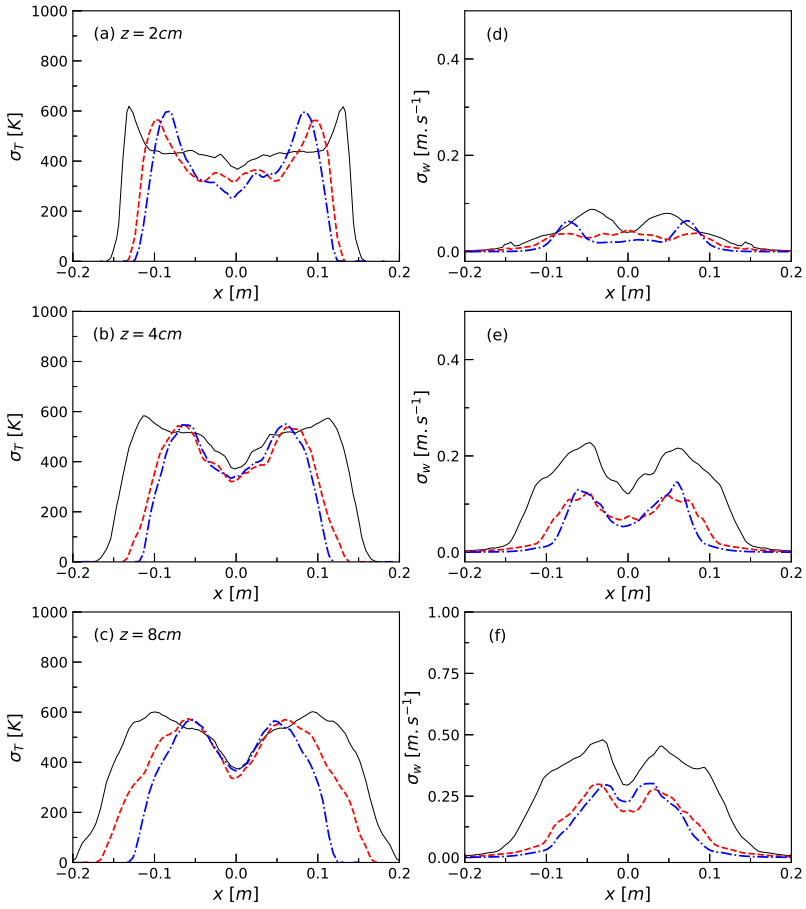

Figure 16: Effects of pool boundary conditions on radial profiles at different heights of rms of temperature and axial velocity.

from the second instability, are significantly smaller than in the NoLip case as observed by comparing Fig. 13e to h with Figs. 14e and f. As a consequence, the pumping capacity is lower in the NoLipNoEnt case which accelarates the formation of a new vortex [63], leading to a flame puffing frequency of 2.97 Hz higher than that of 2.27 Hz observed for the NoLip case. Such increase in the puffing frequency as the air entrainment at the flame base is altered can

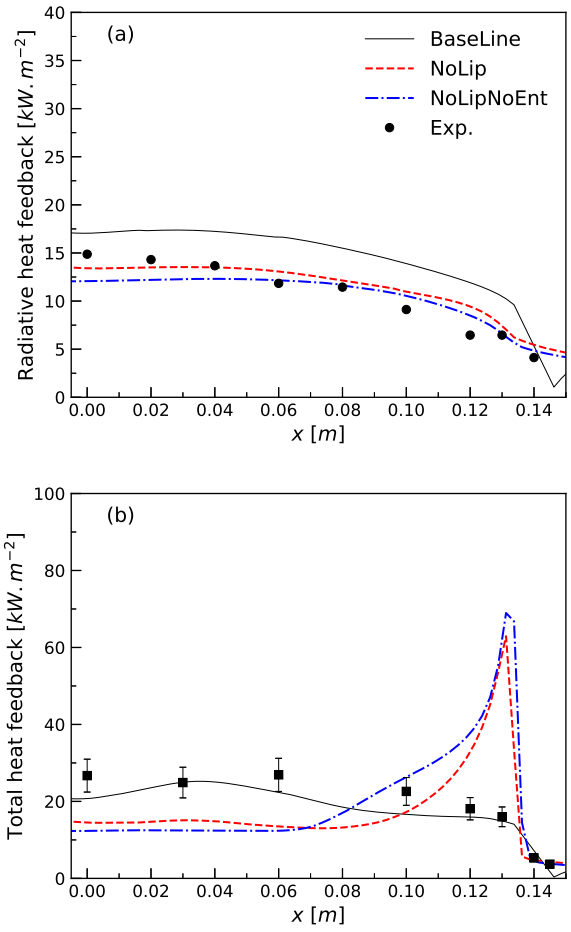

Figure 17: Effects of pool boundary conditions on heat feedback to the pool surface: (a) radiative flux and (b) total flux. The experimental data for radiative and total heat fluxes are taken from Refs. [16] and [18], respectively.

be also observed in the PSD reported by Weckman and Sobiesiak [55] from their experiments in 30 cm acetone pool fires. The fact that air is entrained preferentially from the sides explains also why the fire plume is narrower in the NoLipNoEnt case (see Figs. 15 and 16). On the other hand, the axial

profiles of temperature and velocity are not notably affected, despite that the axial temperature profile is steeper in the continuous flame region for the NoLip case (see Figs. 15).

Figure 17 shows the influence of the fuel boundary conditions on both radiative and total heat feedback to the fuel surface. Before started the discussion, it should be reminded that these predictions have been obtained by considering the fuel burning per unit area unchanged for the different boundary conditions. This figure shows that the heat feedback for the NoLip and the NoLipNoEnt cases are very similar. This is not surprising since these two boundary conditions lead to similar thermal and flow fields (see Figs. 15 and 16). On an opposite way, the inclusion of the fuel Lip height in the simulations (baseline case) induces significant modifications in both radiative and total fluxes. As discussed by Babrauskas [64], the presence of the fuel lip height produces a more emissive flame volume, resulting in a higher radiative flux (see Fig. 17 a). This increase in flame emissivity can be explained by the enhanced mixing process produced by the fuel lip height that leads, as discussed previously, to a wider, hotter, and more turbulent fire at vicinity of the fuel surface (see Figs. 15 and 16). Figure 17b shows that, for the same reasons, the total heat flux for $z < 10$ cm is higher for the baseline case. Close to the burner rim, the total heat fluxes predicted for the NoLip and NoLipNoEnt cases increases sharply owing to an increase in the convective flux. This increase in convection results from the higher proximity between the flame sheet and the fuel surface at the edge of the burner in these configurations. This is not observed for the baseline case where the flame sheet is anchored at the top of the burner rim, leading to

lower temperature at vicinity of the fuel surface. This increasing importance of convection close to the edge of the pool in absence of fuel lip height is supported by the experimental results of Hamins et al. [16] who observed a similar trend as the fuel lip height was reduced from 0.5 cm to 0.1 cm.

4. Conclusions

LES of 30 cm diameter methanol pool fires was performed using state-of-the-art SGS models for mixing, combustion and thermal radiation. A special attention was paid to the effects of the burner boundary conditions on the dynamics of the pool fire. The following conclusions can be drawn:

1. An exhaustive comparison with experiments was carried out in terms of puffing frequency, mean and rms temperature and velocities, mean molar fractions of major species and radiative loss to the surrounding. Numerical simulations were found to reproduce the experimental data with fidelity without introducing any adjustable constant.

2. Considering a non-zero lip height alters substantially the flow structure and results in significantly wider fire flumes and shorter flames which affects both radiative and total heat feedback to the fuel surface.

3. Considering that the burner rim is floor flush has a moderate influence on the fire pool structure as compared to the NoLip case but enhances significantly the puffing frequency owing to a reduction in the pumping capacity of the large-scale vortices.

4. These results show clearly that the experimental burner boundary con-

ditions have to be reproduced scrupulously in the simulations for relevant validations of numerical models.

Acknowledgements

JLC wishes to express his gratitude to Electricité de France (EDF) for financial supports.

References

[1] K. McGrattan, S. Hostikka, R. McDermott, J. Floyd, C. Weinschenk, K. Overholt, Dynamics Simulator Technical Reference Guide Volume 1: Mathematical model, NIST Special Publication 1018 6th Edition, 2014.

[2] FireFoam, `http://code.google.-com/p/firefoam-dev/`.

[3] The 1st Measurement and Computation of Fire Phenomena (MaCFP) Workshop, 2017, `http://www.iafss.org/macfp/`.

[4] B.J. McCaffrey, Purely buoyant diffusion flames some experimental results, NBSIR 79-1910, NIST, 1979.

[5] G. Cox, R. Chitty, A study of the deterministic properties of unbounded fire plumes, Combust. Flame, 39 (1980) 191–209.

[6] G. Cox, R. Chitty, Some stochastic properties of fire plumes, Fire Mater., 6 (1982) 127–134.

[7] G. Cox, R. Chitty, Some source-dependent effects of unbounded fires, Combust. Flame, 60 (1984) 219–232.

[8] N.L. Crauford, S.K. Liew, J.B. Moss, Experimental and numerical simulation of a buoyant fire, Combust. Flame, 31 (1985) 63–77.

[9] S.J. Fischer, B. Hardouin-Duparc, W.L. Grosshandler, The structure and radiation of an ethanol pool fire, Combust. Flame, 70 (1987) 291–306

[10] E.J. Weckman, A. Sobiesiak, The oscilatory behaviour of medium-scale pool fires, Symp. (Int.) Combust., 22 (1988) 1299–1310

[11] M. Klassen, J.P. Gore, Structure and radiation properties of pool fires, NIST-GCR-94-651, NIST, 1992.

[12] E.J. Weckman, A.B. Strong, Experimental investigation of the turbulence structure of medium-scale methanol pool fires, Combust. Flame, 27 (1996) 87–88.

[13] S.R. Tieszen, T. O'Hern, E.J. Weckman, R.W. Schefer, Experimental study of the effect of fuel mass flux on a 1-m-diameter methane fire and comparison with a hydrogen fire, Combust. Flame, 139 (2004) 126–141.

[14] T.K. Blanchat, V.F. Nicolette, W.D. Sundberg, V.G. Figueroa, Well-characterized open pool experiment data and analysis for model validation and development, SAND2006-7508, Sandia National Laboratories, Albuquerque, NM, USA, 2006.

[15] T.K. Blanchat, J. Suo-Anttila, Hydrocarbon characterization experiments in fully turbulent fires - results and data analysis, SAND2010-6377, Sandia National Laboratories, Albuquerque, NM, USA, 2010.

[16] A. Hamins, S.J. Fischer, T. Kashiwagi, M.E. Klassen, J.P. Gore, Heat feedback to the fuel surface in pool fires, Combust. Sci. Technol, 97 (1994) 37–62.

[17] A. Hamins, A. Lock, The Structure of a Moderate-Scale Methanol Pool Fire, NIST Technical Note 1928, 2016.

[18] S.C. Kim, K.Y. Lee, A. Hamins, Energy balance in medium-scale methanol, ethanol, and acetone pool fires, Fire Safety J., 107 (2019) 44–53.

[19] K. Sung, J. Chen, M. Bundy, M. Fernandez, A. Hamins, The Thermal Character of a 1 m Methanol Pool Fire, NIST Technical Note 2083, 2020.

[20] P.E. Desjardin, Modeling of conditional dissipation rate for flamelet models with application to large eddy simulation of fire plumes, Combust. Sci. Technol., 177 (2005) 1883–1916.

[21] Y. Xi, J.P. Gore, K.B. McGrattan, R.G. Rehm, H.R. Baum, Fire dynamics simulation of a turbulent buoyant flame using a mixture-fraction-based combustion model, Combust. Flame, 141 (2005) 329–335.

[22] S.C.P. Cheung, G.H. Yeoh, A fully-coupled simulation of vortical structures in a large-scale buoyant pool fire, Int. J. Therm. Sci., 48 (2009) 2187-2202.

[23] Y. Wang, P. Chatterjee, J.L. de Ris, Large Eddy Simulation of fire plumes, Proc. Combust. Inst., 33 (2011) 2473–2480.

[24] Z. Chen, J. Wen, B. Xu, S. Dembele, Large Eddy Simulation of fire dynamics with the improved eddy dissipation concept, Fire Safety Science-Proc. 10th Int. Symp., (2011) 795–808.

[25] Z. Chen, J. Wen, B. Xu, S. Dembele, Large Eddy Simulation of a medium-scale methanol pool fire using the extended eddy dissipation concept, Int. J. Heat Mass Transf., 70 (2014) 389–408.

[26] Z. Chen, J. Wen, B. Xu, S. Dembele, Extension of the eddy dissipation concept and smoke point soot model to the LES frame for fire simulations, Fire Safety J., 64 (2014) 12–26.

[27] P. Chatterjee, Y. Wang, K.V. Meredith, S.B. Dorofeev, Application of a subgrid soot radiation model in the numerical simulation of a heptane pool fire, Proc. Combust. Inst., 35 (2015) 2573–2580.

[28] G. Maragkos, T. Beji, B. Merci, Advances in modelling in CFD simulations of turbulent gaseous pool fires, Combust. Flame, 181 (2017) 22–38.

[29] G. Maragkos, T. Beji, B. Merci, Towards predictive simulations of gaseous pool fires, Proc. Combust. Inst., 37 (2019) 3927–3934.

[30] G.C. Fraga, F.R. Centeno, A.P. Petry, P.J. Coelho, F.H.R. França, On the individual importance of temperature and concentration fluctuations in the turbulence-radiation interaction in pool fires, Int. J. Heat Mass Transf., 136 (2019) 1079–1089.

[31] I. Sikic, S. Dembele, J. Wen, Non-grey radiative heat transfer modelling in LES-CFD simulated methanol pool fires, J. Quant. Spectrosc. Radiat. Transf., 234 (2019) 78–89.

[32] B. Wu, S.P. Roy, X. Zhao, Detailed modeling of a small-scale turbulent pool fire, Combust. Flame, 214 (2020) 234–237,

[33] A. Wang, M.F. Modest, Photon Monte Carlo simulation for radiative transfer in gaseous media represented by discrete particle fields, J. Heat Transf., 128 (2006) 1041–1049.

[34] L. Orloff, Simplified radiation modeling of pool fires, Symp. (Int.) Combust., 18 (1981) 549–561.

[35] L. Orloff, J.L. de Ris, Froude modeling of pool fires, Symp. (Int.) Combust., 19 (1982) 885–895.

[36] B.B. Ditch, J.L. de Ris, T.K. Blanchat, M. Chaos, R.G. Bill Jr, S.B. Dorofeev, Pool fires - An empirical correlation, Combust. flame, 160 (2013) 2964–2974.

[37] P. Moin, K. Squires, W. Cabot, S. Lee, A dynamic subgrid-scale model for compressible turbulence and scalar transport, Phys. Fluids A, 3 (1991) 2746–2757.

[38] D.K. Lilly, A proposed modification of the Germano subgrid-scale closure method, Phys. Fluids A, 4 (1992) 633–635.

[39] D. Carbonell, C.D. Perez-Segarra, P.J. Coelho, A. Oliva, Flamelet mathematical models for non-premixed laminar combustion, Combust. Flame, 156 (2009) 334–347.

[40] M. Ihme, H. Pitsch, Modeling of radiation and nitric oxide formation in turbulent nonpremixed flames using a flamelet/progress variable formulation, Phys. Fluids, 20, 055110, 2008.

[41] R. Xu, V.M. Le, A. Marchand, S. Verma, T. Rogaume, F. Richard, J. Luche, A. Trouve, Simulations of the coupling between combustion and radiation in a turbulent line fire using an unsteady flamelet model, Fire Safety J., 2020

[42] A.E. Lutz, R.J. Kee, J.F. Grcar, F.M. Rupley, OPPDIF: a FORTRAN program for computing opposed-flow diffusion flames, SAN96-824, Sandia National Laboratories, Albuquerque, NM, USA, 1996.

[43] H. Pitsch, N. Peters, A consistent flamelet formulation for non-premixed combustion considering differential diffusion effects, Combust. Flame, 114 (1998) 26–40.

[44] J. Li, Z. Zhao, A. Kazakov, M. Chaos, F.L. Dryer, J.J. Scire Jr., A comprehensive kinetic mechanism for CO, CH_2O, and CH_3OH combustion, Int. J. Chem. Kinetics, 39 (2007) 109–136.

[45] T. Echekki, E. Mastorakos, Turbulent Combustion Modeling. Advances, New Trends and Perspectives, Springer Verlag, New York, 2010.

[46] F. Nmira, L. Ma, J.L. Consalvi, Assessment of subfilter-scale turbulence-radiation interactions in non-luminous pool fires, Proc. Combust. Inst., 2020.

[47] C.D. Pierce, P. Moin, Progress-variable approach for Large Eddy Simulation of non-premixed turbulent combustion, J. Fluid Mech., 504 (2004) 73–97.

[48] C. Jiménez, F. Ducros, B. Cuenot, B. Bédat, Subgrid scale variance and dissipation of a scalar field in Large Eddy Simulations, Phys. Fluids, 13 (2001) 1748–1754.

[49] V.P. Solovjov, B.W. Webb, F. Andre, The rank correlated FSK model for prediction of gas radiation in non-uniform media, and its relationship

to the rank correlated SLW model, J. Quant. Spectrosc. Radiat. Transf., 214 (2018) 120–132.

[50] M.F. Modest, R.J. Riazzi, Assembly full spectrum k-distribution from a narrow band database: effects of mixing gases, gases and non-gray absorpting particles and non-gray scatters in non-gray enclosures, J. Quant. Spectrosc. Radiat. Transf., 90 (2005) 169–189.

[51] L.S. Rothman, I.E. Gordon, R.J. Barber, H. Dothe, R.R. Gamache, A. Goldman, V.I. Perevalov, S.A. Tashkun, J. Tennyson, HITEMP: the high-temperature molecular spectroscopic database, J. Quant. Spectrosc. Radiat. Transf., 111 (2010) 2139–2150.

[52] M.F. Modest, Radiative Heat Transfer, Third edition, Academic Press, New York, 2013.

[53] L. Ma, F. Nmira, J.L. Consalvi, Verification and validation of a variableâdensity solver for fire safety applications, Numer. Heat Transf., Part B: Fund., 76 (2019) 107–129.

[54] Code_Saturne, `http://www.code-saturne.org`.

[55] E.J. Weckman, A. Sobiesiak, Processing effects in simultaneous velocity and temperature measurements in an intermittent combusting flow, NATO/ASI on Instrumentation for Combustion and Flow in Engines, 1987.

[56] J.W. Williamson, A.W. Marshall, A. Trouve, Developing extinction criteria for fires, Int. Interflam Conf. 11th Proc., 2007.

[57] S.B. Pope, Turbulent flows, Cambridge University Press, 2000.

[58] K.A. Jensen, J.F. Ripoll, A.A. Wray, D. Joseph, M. El Hafi, On various modeling approaches to radiative heat transfer in pool fires, Combust. Flame, 148 (2007) 263–279.

[59] K. Wakatsuki, G.S. Jackson, A. Hamins, M.R. Nyden, Effects of fuel absorption on radiative heat transfer in methanol pool fires, Proc. Combust. Inst., 31 (2007) 2573–2580.

[60] S.R. Tieszen and L.A. Gritzo, Chapter 2. Transport phenomena that affect heat transfer in fully turbulent fires, in Transport Phenomena in Fire, M. Faghri and b. Suden (Eds.), 2008, 25–68, WIT Press, Southampton.

[61] B.M. Cetegen, T.A. Ahmed, Experiments on the periodic instability of buoyant plumes and pool fires, Combust. Flame, 93 (1993) 157–184.

[62] B.M. Cetegen, A phenomenological model of near-field entrainment, Fire Safety J., 31 (1998) 299–312.

[63] L. Hu, J. Hua, J.L. de Ris, Flame necking-in and instability characterization in small and medium pool fires with different lip heights, Combust. Flame, 162 (2015) 1095–1103.

[64] V. Babrauskas, Estimating Large Pool Fire Burning Rates, Fire Technol., 19 (1983) 251–261.